sistent for periods of several months and correspond to known anomalous periods in the oceanic and atmospheric climate. If the mean sea level difference between the topographic ridge and trough is set arbitrarily at 20 cm, the highest difference (50 cm) is observed in December 1957, when a strong El Niño developed off Peru (*9*). Also the 12-month running mean of the sea level difference fluctuates considerably between a high value of 33 cm in January 1958 and a low value of 10 cm in June 1970 and July 1955, the latter recognized as a cold year in the North Pacific (*10*).

Since the countercurrent transports warm water from the western Pacific Ocean into the eastern tropical Pacific, a strong flow in the countercurrent should lead to an accumulation of warm surface water off the coast of Central America. To study this hypothesis, sea surface temperature anomalies in the triangle formed by the coast of Central America, 100°W longitude, and 10°N latitude were averaged. The data have been published in the form of average monthly anomalies for 2-degree squares (*11*). The time series of these surface temperature anomalies for individual months and the 12-month running mean are shown in Fig. 2. They correlate well with the countercurrent transport ($r = 0.79$) for the 12-month running means.

The high correlation between the transport of the countercurrent, as inferred from the observed sea level difference across it, and the sea surface temperature anomaly off Central America points to a causal relationship: strong transports in the countercurrent cause an accumulation of warm water in the eastern tropical Pacific. The peaks in the curve of the individual monthly values—especially in the last decade, when observations of sea surface temperatures were more numerous and the averages more reliable—indicate that a positive temperature anomaly follows a peak in the countercurrent transport by about 3 months. This means that the countercurrent must be strong for an appreciable period of time before an effect on the surface temperature in the eastern Pacific Ocean becomes evident, so that it may be possible to use observed sea level differences to predict temperature trends thousands of kilometers downstream. Bjerknes (*9*) has stressed the importance of the accumulation of large amounts of warm water in the eastern tropical Pacific as a prerequisite for the formation of El Niño. One should not, however, disregard the possibility that extremes in both the sea surface temperature and the countercurrent transport are simultaneously associated with an anomaly of oceanic and atmospheric circulation over a much larger part of the Pacific.

The major peaks in the strength of the countercurrent are followed by documented occurrences of El Niño off Peru. The most pronounced event is the well-documented El Niño of 1957 and 1958 which coincided with a strong countercurrent transport (*12*). El Niño in 1953–1954 is mentioned by Posner (*13*), and the abnormally warm temperatures of Central America in 1965–1966 and in 1969 are both described as El Niño in the monthly bulletins of the fishery-oceanography center in La Jolla (*11*). The peak in countercurrent transport of 1963–1964 was probably too weak to produce El Niño, and so was the peak in 1951–1952, which apparently did not lead to El Niño, although Schell (*14*) includes the data from that year in a study of abnormally warm conditions off Peru.

The foregoing demonstrates that changes in the transport of the equatorial countercurrent decisively affect the temperature distribution in the eastern tropical Pacific, and are strongly linked with such climatic abnormalities as El Niño. It is significant that the transport of a major ocean current can be monitored by very simple measurements such as those of sea level, and this fact emphasizes the importance of obtaining long time series representative of climatic fluctuations.

KLAUS WYRTKI
Department of Oceanography, University of Hawaii, Honolulu 96822

References and Notes

1. El Niño is a flow of warm tropical surface water which in some years extends over the cooler waters along the coast of Peru. Its biological consequences lead to a mass mortality of fish and sea birds. It is named El Niño (The Child) because it occurs after Christmas.
2. J. Bjerknes, *Mon. Weather Rev.* **97**, 163 (1969).
3. J. A. Knauss, in *The Sea*, M. N. Hill, Ed. (Interscience, New York, 1963), vol. 1, pp. 235–252.
4. J. L. Reid, *Tellus* **13**, 489 (1961).
5. K. Wyrtki and R. Kendall, *J. Geophys. Res.* **72**, 2073 (1967).
6. R. Kendall, dissertation, Nova University, Fort Lauderdale, Florida (1970).
7. The values of monthly mean sea level were obtained from the National Ocean Survey, National Oceanic and Atmospheric Administration, Rockville, Maryland.
8. "Atlas of surface currents, northwestern Pacific Ocean," *U.S. Navy Hydrogr. Off. Publ. 569* (1953).
9. J. Bjerknes, *Bull. Inter.-Amer. Trop. Tuna Comm.* **5**, 219 (1961).
10. M. Rodewald, *Deut. Hydrogr. Z.* **11**, 78 (1958).
11. *Fishing Information*, issued monthly by National Marine Fisheries Service, La Jolla, California.
12. T. S. Austin, *Calif. Coop. Oceanic Fish. Invest. Rep.* **7**, 52 (1960).
13. G. S. Posner, *Bull. Bingham Oceanogr. Collect. Yale Univ.* **16**, 105 (1957).
14. I. I. Schell, *J. Geophys. Res.* **70**, 5529 (1965).
15. Supported by the National Science Foundation and the Office of Naval Research under the North Pacific Experiment of the International Decade of Ocean Exploration; this support is gratefully acknowledged. Hawaii Institute of Geophysics Contribution No. 514.

7 December 1972; revised 26 January 1973

Lunar Cinder Cones

Abstract. *Data on terrestrial eruptions of pyroclastic material and ballistic considerations suggest that in the lunar environment (vacuum and reduced gravity) low-rimmed pyroclastic rings are formed rather than the high-rimmed cinder cones so abundant on the earth. Dark blanketing deposits in the Taurus-Littrow region (Apollo 17 landing area) are interpreted as being at least partly composed of lunar counterparts of terrestrial cinder cones.*

Mantling deposits with low albedos (.074 to .085) (*1*) have been mapped in several regions of the moon (Aristarchus Plateau, Copernicus CD, the Rima Bode area, Alphonsus, Sulpicius Gallus, Littrow, and north of Hyginus) and have generally been interpreted as pyroclastics because of their low albedos and smooth surfaces and the way that they subdue underlying terrain (*2*). Possible lunar pyroclastic cones have been described in other areas, most notably in the Marius Hills (*3*). However, a puzzling aspect of the dark mantle deposits is that they do not appear to be associated with cinder cones of the size and type of those found amid, and constituting the source of, terrestrial pyroclastic deposits. As they often mantle relatively young deposits, these units may represent some of the youngest stages of igneous activity recognized on the lunar surface. An area in the dark mantle near the crater Littrow (Fig. 1A) was chosen as the landing site for the Apollo 17 mission, and a primary objective of the mission was to explore and sample the low-albedo material.

Before Apollo 17, significant new information relevant to the nature of the sources of these dark mantle deposits

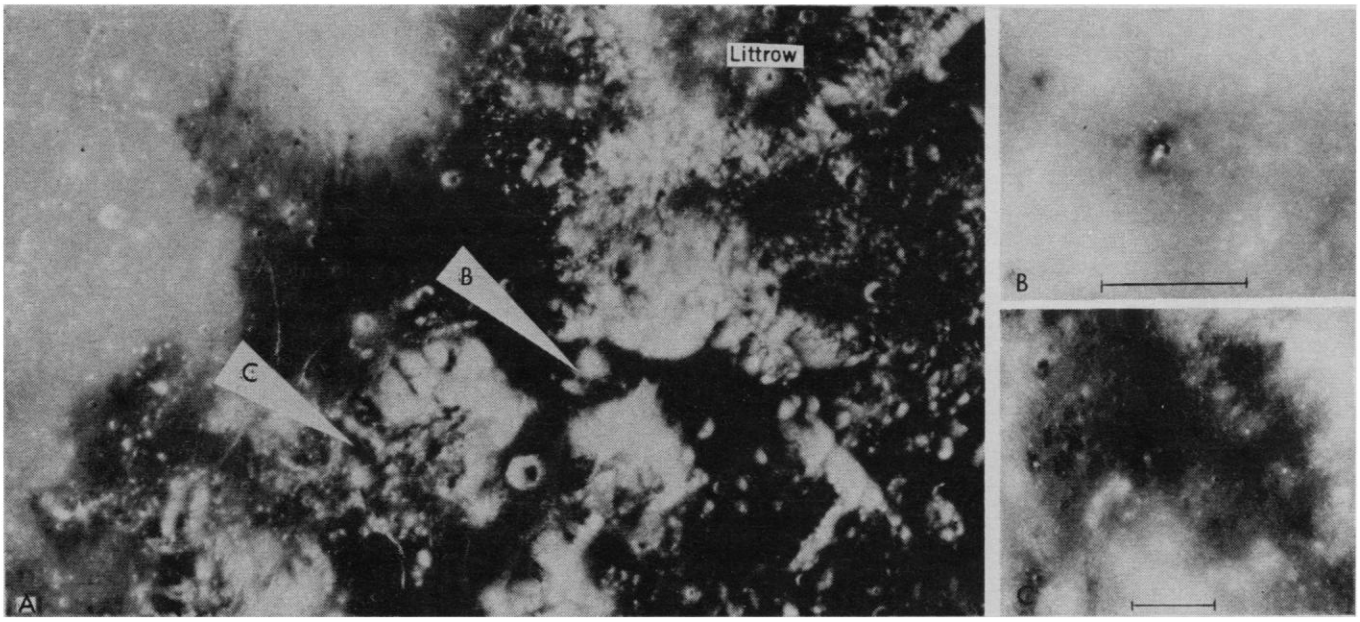

Fig. 1. (A) Taurus-Littrow region of the moon; the frame width is 120 km. The dark mantle is seen around the crater Littrow, particularly to the southwest, where it is continuous. The arrows point to two of the most prominent examples of dark-haloed craters in the region, which are shown enlarged in (B) and (C) (scale bar, 1 km). The Apollo 17 landing site is about 13 km east of the tip of the right arrow. [This is a portion of NASA photograph AS15-M3-0972]

was obtained from (i) observations of the Littrow region from lunar orbit by Apollo 15 astronaut Worden (*4*), (ii) very-high-resolution photographs of the Taurus-Littrow area, and (iii) studies of the physical geology and ballistics of ejecta from terrestrial cinder cones at Mount Etna and Stromboli (Italy) (*5*). Information from the Apollo 17 mission is presently undergoing study and will be treated separately.

The crater Littrow is on the southeastern edge of Mare Serenitatis, southwest of the Taurus Mountains. The continuous dark mantle deposit so conspicuous on photographs of this region (Fig. 1A) is generally southwest of Littrow. It covers an area of approximately 1750 km^2 and rests on the flat, low-lying plains which are marginal to Serenitatis and embay the valleys separating the mountains around the basin edge. Patchy, discontinuous deposits of dark mantle occur in much of the mountainous region in the central and eastern parts of the area shown in Fig. 1A. The combined area occupied by these deposits and the continuous dark mantle is over 6000 km^2.

The high-inclination lunar orbit required to land in the Hadley-Apennine area (latitude 26°N), target of the Apollo 15 mission, carried a manned spacecraft over the Littrow area for the first time. During several passes over the dark-mantled region, Worden described numerous features with generally symmetric dark halos, which he interpreted as cinder cones (*4*). Examination of the returned high-resolution (approximately 2 m) photographs showed the numerous, low-rimmed craters with dark halos described by Worden and also indicated that the continuous dark mantle was a smooth deposit. The thickness of the deposit was estimated to average about 10 to 15 m on the basis of the depth to which premantle structures were filled and the size of postmantle craters. Most of these dark-haloed craters have extremely low or undetectable rims, and in the continuous dark mantle they appear to be randomly distributed. The details of their structure are obscured

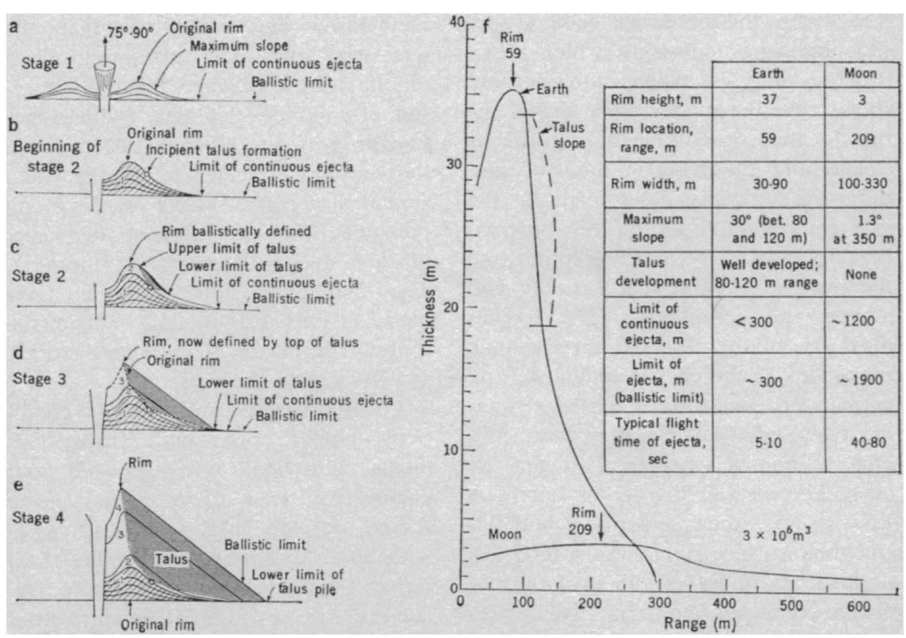

	Earth	Moon
Rim height, m	37	3
Rim location, range, m	59	209
Rim width, m	30-90	100-330
Maximum slope	30° (bet. 80 and 120 m)	1.3° at 350 m
Talus development	Well developed; 80-120 m range	None
Limit of continuous ejecta, m	< 300	~ 1200
Limit of ejecta, m (ballistic limit)	~ 300	~ 1900
Typical flight time of ejecta, sec	5-10	40-80

Fig. 2. Idealized stages of evolution of terrestrial cinder cones (a to e) and an actual terrestrial cone scaled to lunar conditions (f). (a) Stage 1 is a low-rimmed pyroclastic ring. (b and c) Stage 2 begins with the development of exterior talus. (d) Stage 3 begins with the destruction of the original rim by inward migration of the talus pile. (e) In stage 4 the cone grows beyond the ballistic limit of ejecta. Lunar cinder cones probably only rarely evolve past stage 1 (a), as suggested by (f) cinder cone profiles for the earth and the moon calculated on the basis of the cone volume, exit velocity, and launch angles observed at Northeast Crater on Mount Etna. The detailed properties of these model cones are summarized in the inset.

by the dark background, but in the patchy deposits a number of isolated cones and individual haloed craters can be seen (Fig. 1, B and C); these offer the best opportunity for analysis of the characteristics of individual dark-haloed craters.

The application of terrestrial field experience on pyroclastic cones and considerations of ballistics permit some inferences to be made about the origin of these lunar features. Terrestrial pyroclastic eruptions at Stromboli and Mount Etna were photographed with time exposures and in high-speed 70-mm movies, and the data obtained have provided quantitative information on the size, flux, and velocity of ejected particles and on the evolution of some typical terrestrial cinder cones (*5*). Northeast Crater, near the summit of Mount Etna, originated in 1911 and has grown to its present volume (3×10^6 m^3) through many small similar eruptive events, each of which contributes about 0.5 m^3 of new material. Photographs of Northeast Crater eruptions show that fragments exit at a median velocity of 51 m/sec at angles from 70° to vertical. High-speed movies of Stromboli also show median exit velocities near 50 m/sec.

Quantitative models of the growth of cinder cones through the superposition of the ejecta from repeated eruptions of this type are in good agreement with the observed cone shapes (*5*). Ballistic analysis in which atmospheric drag is taken into account shows that the cinder cone shape, the rim location, the limit of continuous ejecta, and the ballistic limit of particles are uniquely determined by the exit conditions (eruption velocity and launch angle), the cone volume, and the ballistic environment (gravity and atmospheric conditions). The models make use of the observed aerodynamic properties of the ejecta, which at Etna consists of a mixture of particles ranging from ash (particle size, about 150 μm) to bombs (median diameter, 15 cm). The median density of bombs is 1.53 g/cm^3, their sphericity is 0.78, and their surface roughness is 0.05 (*5*).

Idealized stages of the evolution of cinder cones are shown in Fig. 2, a to e (*5*). Typically, cinder cones grow from many small, geyser-like eruptions, each contributing 1 m^3 or less to the cone (called Strombolian activity). Many repeated eruptions of this type will produce a sequence of morphological features which vary as the cone volume increases. At stage 1 the cone is a low-rimmed pyroclastic ring consisting of layers of ejecta in similar beds. Stage 2 begins when the outside slope of the cone reaches the angle of repose and talus develops. As the cone grows in volume the limits of the talus slope migrate both upward and downward. Eventually the talus pile migrates inward through the original flat rim, defining the onset of stage 3. With continued growth the lower limit of the talus slope migrates beyond the ballistic limit of ejected particles. The properties of the cone shapes are quantitatively defined by the cone volume, exit conditions, and ballistics. Terrestrial cinder cones of all stages are observed, but lunar cones probably only rarely evolve beyond stage 1 because the material is so widely dispersed ballistically.

If an average eruption of Etna's Northeast Crater (a typical terrestrial cinder cone) occurred on the moon, the effects of lack of atmospheric drag and decreased gravity would combine to increase the radius of dispersion and the ejecta flight times. If allowed to accumulate to a volume similar to that of Northeast Crater (3×10^6 m^3), the resulting cinder cone would have a strikingly different shape, as shown in Fig. 2f. The ballistic limit and the limit of continuous ejecta on the moon are in excess of six times those on the earth. The lunar cone has a considerably lower and wider rim than the terrestrial one. The maximum slope on the terrestrial cone forms as a result of talus development (with slopes of 30° between 80 and 120 m from the center of the vent), but the widespread dispersal of ejecta on the moon precludes the development of steep, unstable slopes (for these volumes). The maximum slope of this lunar model is only 1.3° at 350 m from the center. The details of the above models are developed elsewhere (*5*).

To summarize, under lunar conditions, cinder cones built from fragments with exit velocities and exit angles like those of terrestrial ejecta should develop into pyroclastic rings with low to barely discernible rims, rather than a cluster of discrete isolated cones so familiar in terrestrial volcanic fields. Lunar flight times are typically of the order of 1 minute, so that cooling times will be longer and ejecta generally should not be welded.

A variety of dark, low-rimmed craters exist in the discontinuous dark mantle of the Taurus-Littrow area. One of the most distinctive and highest-rimmed haloed craters in the area (Fig. 1B) has a crater diameter of 100 m and a rim height probably less than 10 m (*6*). There is a distinct break in slope at a radius of 150 to 200 m, and the limit of continuous ejecta ranges 600 to 800 m from the center of the crater. These data suggest a maximum average slope of about 5° for this cone.

The morphology of this feature approaches that of terrestrial cones, but this is the most distinct structure in the region. Figure 1C illustrates a more typical example of a very-low-rimmed, broad dark-haloed crater with a central crater diameter of about 300 m, an indistinct break in slope at a radius of about 450 m, and an approximate limit of continuous ejecta at a range of 1600 m. The crispness of the central crater and the general sparseness of superposed craters suggest that the morphology of this structure has not been modified by subsequent impacts.

By assuming a pyroclastic origin for these lunar features, a direct comparison can be made with Etna's Northeast Crater, a fairly typical terrestrial cinder cone, as it might form in lunar conditions, by using the numerical models described above. The calculated shape of Northeast Crater in lunar conditions (Fig. 2f) is a flat, low-rimmed cone, similar in form to the lunar features shown in Fig. 1. Agreement between a calculated model and the observed lunar cone shown in Fig. 1B would be excellent for eruption conditions somewhat less vigorous than those at Northeast Crater, perhaps more like those of a terrestrial spatter cone. The low-rimmed cone shown in Fig. 1C would result from eruptions similar to but slightly more vigorous than those at Etna.

In conclusion, we believe that many lunar dark-haloed craters are the lunar counterparts of terrestrial cinder cones with the differences in morphology attributable to differences in environment. The dark blanketing deposits in the Taurus-Littrow region are interpreted to be composed, at least in part, of pyroclastic material ejected from very-low-rimmed craters, which are inferred to be volcanic vents.

THOMAS R. MCGETCHIN
Department of Earth and Planetary Sciences, Massachusetts Institute of Technology, Cambridge 02139
JAMES W. HEAD
Department of Geological Sciences, Brown University, Providence, Rhode Island 02912

References and Notes

1. H. A. Pohn and R. L. Wildey, *U.S. Geol. Surv. Prof. Pap. 599-E* (1970).
2. D. E. Wilhelms and J. F. McCauley, geologic map of the near side of the moon, *U.S. Geol. Surv. Map I-703* (1971); F. El-Baz, in *NASA Spec. Publ. 289* (1972), p. 25-66; M. H. Carr, in *ibid.*, p. 25-63.
3. T. N. V. Karlstrom, J. F. McCauley, G. A. Swann, U.S. Geological Survey open-file report (1968); J. F. McCauley, *Trans. Amer. Geophys. Union* **50**, 229 (1969); D. H. Scott and N. J. Trask, *U.S. Geol. Surv. Prof. Pap. 599-I* (1971).
4. F. El-Baz and A. M. Worden, *NASA Spec. Publ. 289* (1972), p. 25-1.
5. T. R. McGetchin, M. Settle, B. Chouet, *Trans. Amer. Geophys. Union* **53**, 533 (1972); *J. Geophys. Res.*, in press.
6. S. S. C. Wu, F. J. Schafer, R. Jordan, G. Nakata, J. Derick, in *NASA Spec. Publ. 289* (1972), p. 25-36; U.S. Army Topographic Command, preliminary topographic map of the Apollo 17 landing area (1 : 50,000; zone 36) (July 1972).
7. Research supported by NASA grants NGR-22-009-522 and NGR-22-009-637, by the U.S. Geological Survey under NASA contract T5874A (T.R.M.), and by Bell Telephone Laboratories under NASA contract NASW-2377 (J.W.H.). Publication authorized by the director, U.S. Geological Survey.

10 November 1972; revised 3 January 1973

Mechanisms of Trace Metal Transport in Rivers

Abstract. *Trace metals transported by the Amazon and Yukon rivers were analytically partitioned among the transport phases: in solutions, ion exchange, organic materials, metallic coatings, and crystalline solids. The distribution for both rivers is similarly proportioned, with copper and chromium transported mainly in the crystalline solids, manganese in coatings, and iron, nickel, and cobalt distributed equally between precipitated metallic coatings and crystalline solids.*

It is necessary to know the mechanisms of the transport of trace metals in rivers in order to be able to understand their chemical cycles in nature. This knowledge is indispensable in evaluating the fate of trace metals that man, as a polluter, superimposes on the natural system. From the public health viewpoint it is important whether the trace metals are (i) in solution or adsorbed on solids, where they are readily available; (ii) in organic materials or metallic hydroxides, where chemical changes are required before they are released, so that they are less available; or (iii) in the crystal structures of suspended materials, where they are nearly unavailable in nature.

Numerous workers (*1*) have studied trace elements in sea water, especially in the cores of bottom sediments and in manganese nodules. Jenne (*2*) reviewed the status as of 1968 of the chemistry of trace metals in soils, sediments, and freshwaters, pointing out the need for studies of the relative affinity of organic matter compared with iron and manganese oxides for trace elements in stream sediments. Since then, Turekian and co-workers (*3*) have studied the dissolved Ag, Sb, Cr, Co, Rb, Cs, Se, and Mo in several streams, and have conducted adsorption experiments with American Petroleum Institute clay minerals standards in order to calculate the amounts of the metals adsorbed and released in seawater. They also filtered the suspended material (with a filter of pore size 0.45 μm) and analyzed the bulk samples for Cr, Ag, Mo, Ni, Co, and Mn.

In the present study I attempted to evaluate the amounts of Fe, Ni, Cu, Cr, Co, and Mn actually transported by rivers (i) in solution, (ii) by adsorption, (iii) in solid organic material, (iv) as metallic coatings, and (v) in detrital crystalline material.

All the samples of water and suspended sediments obtained for the study reported here were taken from the Amazon and Yukon rivers, at 60 percent of the depth in the main channel, upstream of any influence from salt water; this ensured that the samples were indicative of river transport. The samples from the Amazon River were taken off Macapá, Brazil; those from the Yukon River were taken upstream from Alakanuk, Alaska. All the samples were filtered under pressure within 2 hours after sampling; the filters (pore size, 0.45 μm) had been washed with filtered river water (*4*). The filtered water samples were acidified with redistilled HCl to pH 1.5 and stored in polyethylene bottles previously washed with redistilled HCl. The filtered residue was stored on the filter, preserved with a volatile organic solution (*5*).

The trace metals in solution in the filtered water samples were concentrated by complexing with ammonium pyrrolidine dithiocarbamate, followed by solvent extraction with methyl isobutyl ketone (*6*). The adsorbed cations were removed from the suspended material by using a $1N$ $MgCl_2$ solution (pH 7). To ensure that none of the suspen-

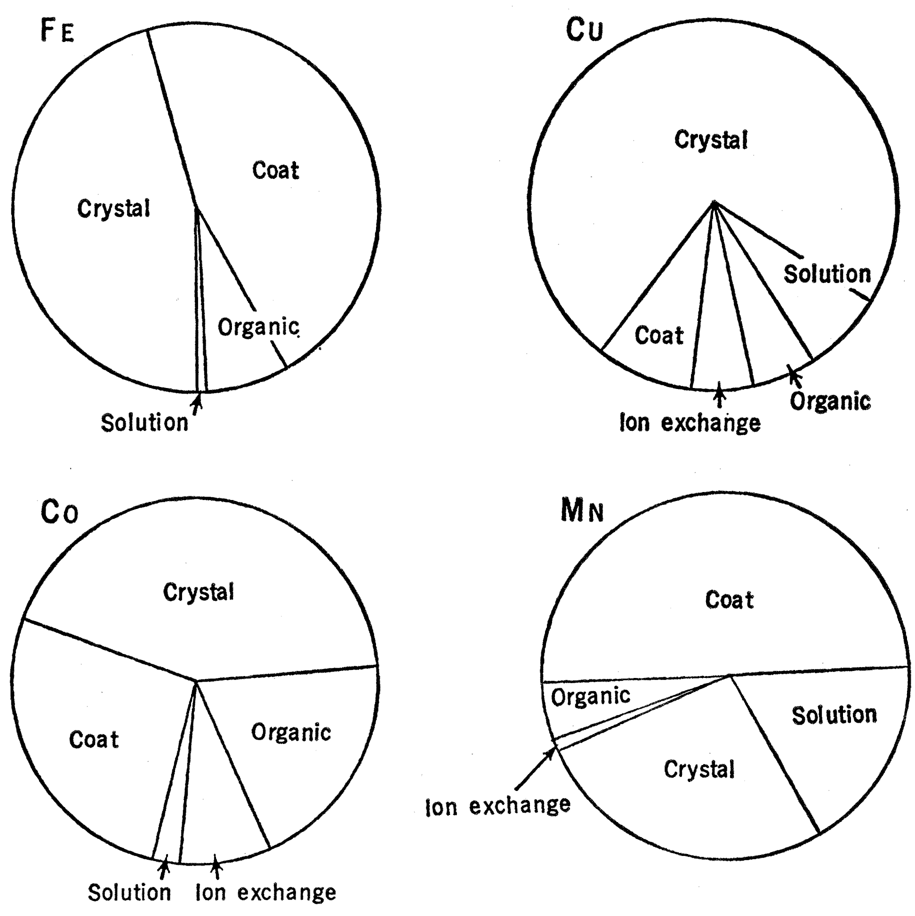

Fig. 1. Relative contributions of five mechanisms involved in transporting Fe, Cu, Co, and Mn in the Amazon River.